

Hearing requires otoferlin-dependent efficient replenishment of synaptic vesicles in hair cells

Tina Pangršič¹, Livia Lasarow², Kirsten Reuter^{3,9}, Hideki Takago^{1,9}, Martin Schwander⁴, Dietmar Riedel⁵, Thomas Frank¹, Lisa M Tarantino⁶, Janice S Bailey⁶, Nicola Strenzke², Nils Brose⁷, Ulrich Müller⁴, Ellen Reisinger³ & Tobias Moser^{1,8}

Inner hair cell ribbon synapses indefatigably transmit acoustic information. The proteins mediating their fast vesicle replenishment (hundreds of vesicles per s) are unknown. We found that an aspartate to glycine substitution in the C₂F domain of the synaptic vesicle protein otoferlin impaired hearing by reducing vesicle replenishment in the *pachanga* mouse model of human deafness DFNB9. *In vitro* estimates of vesicle docking, the readily releasable vesicle pool (RRP), Ca²⁺ signaling and vesicle fusion were normal. Moreover, we observed postsynaptic excitatory currents of variable size and spike generation. However, mutant active zones replenished vesicles at lower rates than wild-type ones and sound-evoked spiking in auditory neurons was sparse and only partially improved during longer interstimulus intervals. We conclude that replenishment does not match the release of vesicles at mutant active zones *in vivo* and a sufficient standing RRP therefore cannot be maintained. We propose that otoferlin is involved in replenishing synaptic vesicles.

At the first auditory synapse in mammals, one ribbon-type active zone of the inner hair cell (IHC) drives one postsynaptic spiral ganglion neuron (SGN) to spike at rates exceeding 100 Hz in silence and 1 kHz on sound onset^{1,2}. Moreover, SGNs sustain firing rates of several hundred hertz during ongoing acoustic stimulation. In such a steady state, vesicle replenishment has to balance vesicle fusion at the IHC active zone. Accordingly, high rates of initial and sustained exocytosis have been found in hair cells^{3–8}. Ribbon-type active zones of IHCs replenish readily releasable vesicles at hundreds of hertz over several seconds of stimulation, faster than ribbon synapses in the eye^{9–15} and most non-ribbon-type active zones¹⁶ (but see ref. 17). This efficient vesicle re-supply maintains a large standing pool of fusion-competent synaptic vesicles, which appears to be critical for reliable and temporally precise sound encoding^{18–20}.

Ca²⁺ stimulates vesicle re-supply at presynaptic active zones^{4,8,21,22}, but the molecular basis underlying the unique replenishment capacity of IHCs remains unclear. One candidate for this function is the multi-C₂ domain protein otoferlin. Otoferlin has been implicated in synaptic vesicle fusion in IHCs²³, as Ca²⁺-dependent exocytosis is largely abolished in IHCs of otoferlin knockout mice (*Otof*^{-/-}), and has been shown to interact with SNARE proteins²³ and Myosin VI^{24,25}.

We studied the effects of a partial loss of otoferlin function from the molecular to the systems level using deaf *pachanga* mice

(*Otof*^{Pga/Pga})²⁶, which carry a *N*-ethyl-*N*-nitrosourea-mediated *Otof* missense mutation (D1767G in NP_001093865, NCBI). Otoferlin protein levels were reduced in IHCs of *Otof*^{Pga/Pga} mice. We explored synaptic transmission at the IHC synapse *in vitro* using pre- or postsynaptic patch clamp, Ca²⁺ uncaging and Ca²⁺ imaging, and *in vivo* by recording auditory-evoked population responses and single neuron spiking. We found that deficient vesicle replenishment underlies the hearing impairment of *Otof*^{Pga/Pga} mice and propose that otoferlin confers the high capacity for vesicle re-supply to the IHC synapse.

RESULTS

Synaptic hearing loss: normal fusion, slowed replenishment

Otof^{Pga/Pga} mice lacked auditory brainstem responses even when probed by very loud sounds (120 dB; **Fig. 1a**), but showed a small potential around the click stimulus, which probably reflected the summed potentials of hair cells. We observed distortion products of otoacoustic emissions with normal amplitude (data not shown), corroborating the notion of intact cochlear amplification²⁶. To further narrow down the site of defect, we studied cochlear function by electrocochleography. Cochlear microphonics, reflecting hair cell mechano-electrical transduction, were readily observed with amplitudes comparable to those of wild-type mice (*Otof*^{f+/+}; **Fig. 1b**). The summing potential, which is thought to primarily

¹InnerEarLab, Department of Otolaryngology and Center for Molecular Physiology of the Brain, University Medical Center Göttingen, Göttingen, Germany. ²Auditory Systems Physiology group, Department of Otolaryngology, University Medical Center Göttingen, Göttingen, Germany. ³Molecular Biology of Cochlear Neurotransmission group, Department of Otolaryngology, University Medical Center Göttingen, Göttingen, Germany. ⁴Department of Cell Biology, Institute for Childhood and Neglected Diseases, The Scripps Research Institute, La Jolla, California, USA. ⁵Laboratory of Electron Microscopy, Max Planck Institute for Biophysical Chemistry, Göttingen, Germany. ⁶Department of Psychiatry, University of North Carolina, Chapel Hill, North Carolina, USA. ⁷Department of Molecular Neurobiology, Max Planck Institute of Experimental Medicine and Center for Molecular Physiology of the Brain, Göttingen, Germany. ⁸Bernstein Center for Computational Neuroscience, University of Göttingen, Göttingen, Germany. ⁹These authors contributed equally to this work. Correspondence should be addressed to T.M. (tmoser@gwdg.de) or E.R. (ereisin@gwdg.de).

Received 29 March; accepted 14 May; published online 20 June 2010; doi:10.1038/nn.2578

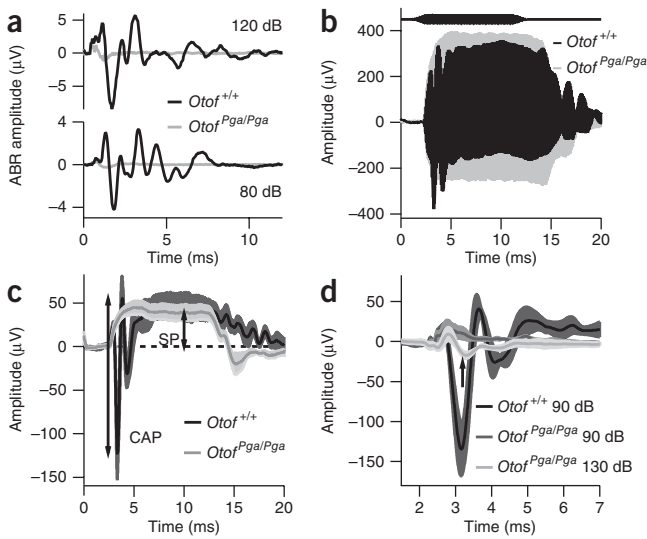


Figure 1 *Otof^{Pgal/Pga}* mice have normal hair cell transduction and receptor potentials, but severe hearing impairment. (a) No auditory brainstem responses (ABR) were elicited by 120-dB (top) and 80-dB (bottom) click stimuli in 2–4-week-old *Otof^{Pgal/Pga}* mice (average traces), whereas normal responses were seen in *Otof^{+/+}* (representative examples) mice. (b) Electrocochleography. Representative traces in response to 12-ms, 90-dB, 12-kHz tone bursts (indicated by top trace) recorded at high bandwidth are shown, illustrating the presence of large cochlear microphonics in *Otof^{Pgal/Pga}* and *Otof^{+/+}* mice. The spiral ganglion compound action potential (CAP, visible for *Otof^{+/+}* at the onset of the tone) is missing in the *Otof^{Pgal/Pga}* mouse. (c) Averages (\pm s.e.m.) of low pass-filtered (3 kHz) electrocochleography traces in response to 12-ms, 90-dB, 12-kHz tone bursts for *Otof^{Pgal/Pga}* and *Otof^{+/+}* mice. We found normal summating potential (SP), but no CAP, in *Otof^{Pgal/Pga}* mice. (d) For clicks at a stimulus level of 130 dB, a small putative negative potential becomes apparent (arrow) in the *Otof^{Pgal/Pga}* mice ($n = 3$), potentially representing a residual spiral ganglion CAP (absent for 90-dB click stimulation).

indicate the summed IHC receptor potential, was maintained in *Otof^{Pgal/Pga}* mice ($48 \pm 15 \mu\text{V}$ for *Otof^{+/+}* and $44 \pm 11 \mu\text{V}$ for *Otof^{Pgal/Pga}*, $n = 6$ each; **Fig. 1c**), suggesting that IHC transduction and basolateral conductance were normal. However, we did not observe obvious compound action potentials even at a click stimulation of 130 dB (**Fig. 1d**). We conclude that the defect causing the hearing impairment of *Otof^{Pgal/Pga}* mice is located downstream of IHC receptor

potential generation, most likely at the IHC synapse. We did not test auditory nerve function by electrical stimulation in *Otof^{Pgal/Pga}* mice, but electrically evoked auditory brainstem responses have been observed in *Otof^{-/-}* mice²³.

Next, we performed patch-clamp measurements of Ca^{2+} currents and membrane capacitance to study presynaptic function in apical IHCs of *Otof^{Pgal/Pga}*, *Otof^{Pgal/-}*, *Otof^{-/-}* and *Otof^{+/+}* mice (**Fig. 2a,b**). Unexpectedly, we found normal exocytic membrane capacitance increments (ΔC_m) for depolarizations lasting up to 10 ms in IHCs of *Otof^{Pgal/Pga}* and *Otof^{Pgal/-}* mice (**Fig. 2b**), indicating normal exocytosis of the RRP⁴ at interstimulus intervals of at least 30 s. We then fitted the

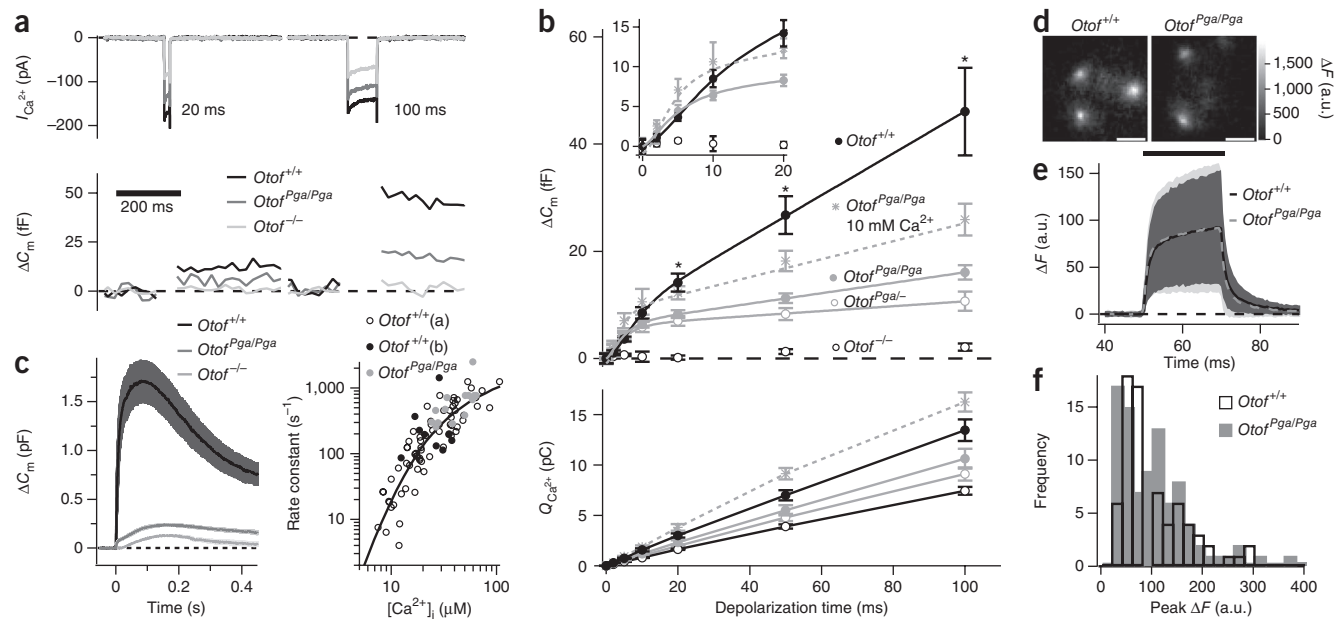


Figure 2 Normal vesicle fusion and impaired vesicle replenishment in *Otof^{Pgal/Pga}* IHCs. (a) Representative Ca^{2+} currents (top) and low pass-filtered C_m changes (bottom) recorded from *Otof^{+/+}*, *Otof^{Pgal/Pga}* and *Otof^{-/-}* IHCs in response to 20-ms (left) and 100-ms (right) depolarizations. (b) Mean (\pm s.e.m.) exocytic ΔC_m (top) and Ca^{2+} current integrals (bottom) of *Otof^{+/+}* ($n = 8$), *Otof^{Pgal/Pga}* ($n = 14$), *Otof^{Pgal/-}* ($n = 13$) and *Otof^{-/-}* ($n = 7$) IHCs as a function of stimulus duration. In addition, data from *Otof^{Pgal/Pga}* IHCs bathed in elevated $[\text{Ca}^{2+}]_i$ (10 mM, $n = 7$) are shown. Lines represent least-square fits to the data (**Table 1**). Inset shows the first 20 ms on an expanded scale. $*P < 0.05$. (c) Average ΔC_m traces (\pm s.e.m.) of *Otof^{+/+}* ($n = 7$), *Otof^{Pgal/Pga}* ($n = 10$) and *Otof^{-/-}* ($n = 7$) IHCs recorded during Ca^{2+} uncaging (0 ms indicates time of flash, see **Table 1** for fit parameters). Right, rate constants of the fast exocytic component as a function of postflash $[\text{Ca}^{2+}]_i$ in *Otof^{Pgal/Pga}* and wild-type IHCs (*Otof^{+/+}*; our data are shown in **b**, data from ref. 48 are shown in **a**). The line represents the fit of a fifth-order model with a cooperativity factor of 0.4 (see ref. 48). (d) Representative hotspots of Fluo-5N fluorescence (Ca^{2+} microdomains) in IHCs of *Otof^{+/+}* and *Otof^{Pgal/Pga}* mice during depolarization to -7 mV. Scale bar represents $2 \mu\text{m}$. (e) Mean and s.d. of background-subtracted Fluo-5N fluorescence recorded by spot detection in the center of the Ca^{2+} microdomain²⁸ (81 domains in 23 *Otof^{+/+}* IHCs, black line and dark gray area, and 88 domains in 24 *Otof^{Pgal/Pga}* IHCs, gray dashed line and light gray area). (f) Distribution of Ca^{2+} microdomain peak ΔF of the same IHCs.



Table 1 Quantification of exocytosis

	Depolarization					
	RRP size (fF, entire IHC) (vesicles per active zone)	τ depletion (ms)	Initial rate (vesicles per s per active zone)	Slope (fF s ⁻¹ , entire IHC)	Sustained rate (vesicles per s per active zone)	Exponent n
<i>Otof</i> ^{+/+} ($n = 8$)	7.0	5.2	2,344	391	679	2.9
<i>Otof</i> ^{Pga/Pga} ($n = 14$)	12	3.9	3,495	98	208	1.6
<i>Otof</i> ^{Pga/Pga} ($n = 7$) 10 mM Ca ²⁺	6.4	2.8	7,117	167	357	2.1
<i>Otof</i> ^{Pga/-} ($n = 13$)	9.4	4.5	2,901	45	97	1.2
	20					
	6.1					
	13					
Ca ²⁺ uncaging						
	Delay (ms)	a_1 (fF)	τ_1 (ms)	a_2 (fF)	τ_2 (ms)	[Ca ²⁺] _i (μ M) n
<i>Otof</i> ^{+/+} ($n = 7$)	1.5 ± 0.5	1,117 ± 144	5.4 ± 1.1	631 ± 127	26 ± 5	28 ± 3 1.7 ± 0.5
<i>Otof</i> ^{Pga/Pga} ($n = 14$)	0.7 ± 0.1	78 ± 11	2.0 ± 0.3	182 ± 8	44 ± 4	43 ± 4 2.9 ± 0.2
<i>Otof</i> ^{-/-} ($n = 7$)	–	–	–	150 ± 13	52 ± 9	52 ± 5 3.1 ± 0.5

Parameters of depolarization-induced exocytosis were estimated by least-squares fitting.

$$\Delta C_m(t) = RRP_size \cdot \left(1 - e^{-t/\tau}\right)^n + slope \cdot t$$

where t denotes the duration of depolarization and τ is the time constant for RRP depletion. The RRP size (in vesicles per active zone) was estimated as the amplitude of the exponential function divided by the product of synapse number and vesicle capacitance (~ 45 aF)⁴⁷. Initial and sustained rates of exocytosis (in vesicles per s per active zone) were calculated from the capacitance data as follows:

Initial rate = RRP size (in fF) ÷ number of synapses ÷ vesicle capacitance ÷ τ , Sustained rate = slope ÷ number of synapses ÷ vesicle capacitance.

Vesicles in electron micrographs from *Otof*^{+/+} and *Otof*^{Pga/Pga} mice were of comparable size (data not shown). Parameters of exocytosis during Ca²⁺ uncaging were estimated by least-squares fitting. For the *Otof*^{+/+} and *Otof*^{Pga/Pga} data,

$$\Delta C_m(t) = a_1 \cdot \left(1 - e^{-\frac{-(t-delay)/\tau_1}{\tau_1}}\right)^n + a_2 \cdot \left(1 - e^{-\frac{-(t-delay)/\tau_2}{\tau_2}}\right)^n$$

For the *Otof*^{-/-} data, $\Delta C_m(t) = a_2 \cdot \left(1 - e^{-t/\tau_2}\right)^n$. Data are presented as mean ± s.e.m. (where available).

mean ΔC_m values obtained for different stimulus durations using the sum of an exponential and a linear function to estimate the amount and kinetics of RRP exocytosis and the rate of sustained exocytosis, respectively (Fig. 2b and Table 1)^{4,27}. RRP size and exocytosis kinetics were normal at active zones of *Otof*^{Pga/Pga} mice (Table 1), in marked contrast with the near-complete lack of RRP exocytosis in IHCs of *Otof*^{-/-} mice (Fig. 2a,b and ref. 23), which showed significant exocytosis only for depolarizations of 100 ms and longer ($P < 0.01$, data from ref. 23).

Moreover, Ca²⁺ uncaging caused a small, fast ΔC_m in *Otof*^{Pga/Pga}, but not in *Otof*^{-/-}, IHCs (Fig. 2c and Table 1). Potential reasons for the marked amplitude reduction of the flash photolysis-induced ΔC_m in *Otof*^{Pga/Pga}, which was still larger than the Ca²⁺ influx-triggered RRP exocytosis by one order of magnitude, could include fewer docked and primed vesicles outside of active zones. The rate constants of the remaining fast component of *Otof*^{Pga/Pga} IHCs at a given postflash intracellular Ca²⁺ concentration ($[Ca^{2+}]_i$) were comparable to those of *Otof*^{+/+} IHCs, which is consistent with the notion of an unaltered Ca²⁺-dependent fusion reaction (Fig. 2c and Table 1). Confocal Ca²⁺ imaging showed IHC synaptic Ca²⁺ microdomains²⁸ with normal amplitude and size as well as near-normal kinetics (Fig. 2d-f and Supplementary Table 1). Thus, we attribute the small reduction of the Ca²⁺ influx in *Otof*^{Pga/Pga} IHCs (20%; Fig. 2a,b) to the similarly decreased number of synapses (19%) assessed by immunohistochemistry (*Otof*^{Pga/Pga}, 10.4 ± 0.7 synapses per IHC, $n = 357$ IHCs; *Otof*^{+/+}, 12.8 ± 0.3 synapses per IHC, $n = 180$ IHCs; Supplementary Fig. 1 and Supplementary Table 2). In summary, our findings indicate that presynaptic Ca²⁺ signaling, RRP size and vesicle fusion are intact at active zones of *Otof*^{Pga/Pga} IHCs under the chosen *in vitro* conditions.

However, beyond 10 ms of depolarization, the capacitance rise proceeded much more slowly in *Otof*^{Pga/Pga} and *Otof*^{Pga/-} IHCs. This sustained exocytosis after release of the RRP is thought to primarily represent the rate-limiting re-supply of vesicles to the RRP and their subsequent fusion during continued Ca²⁺ influx^{5,8,29-31}, but a potential contribution of fusion-competent vesicles that are released more slowly cannot be ruled out. Here, we assumed that sustained exocytosis primarily reports re-supply to the RRP and estimated its rate as the slope of a linear function (fitted to the data of Fig. 2b). The mean vesicle supply was diminished from 700 vesicles per s per active zone in *Otof*^{+/+} to 200 vesicles per s per active zone in *Otof*^{Pga/Pga} and 100 vesicles per s per active zone in *Otof*^{Pga/-} IHCs (Fig. 2b and Table 1). Increasing the Ca²⁺ influx beyond that of *Otof*^{+/+} IHCs by elevating the extracellular Ca²⁺ concentration ($[Ca^{2+}]_e$) enhanced sustained exocytosis in *Otof*^{Pga/Pga} IHCs (360 vesicles per s per active zone). This indicates that the mutation does not abolish the Ca²⁺ dependence of vesicle supply and that the replenishment defect can be partially overcome by increasing Ca²⁺ influx.

The fact that RRP size was normal after resting the synapse for more than 30 s and that vesicle re-supply was reduced during ongoing stimulation prompted us to explore RRP recovery from depletion using paired-pulse experiments (Fig. 3a). RRP recovery, assessed as the paired-pulse ratio for different interpulse intervals, was impaired in *Otof*^{Pga/Pga} mice (Fig. 3b). This suggests that there is also a deficit in vesicle replenishment in the rest period between stimuli. Trains of ten short (10 ms) depolarizations, applied after a period of rest (30-s voltage clamp at -84 mV), elicited a ΔC_m pattern that was indicative of normal RRP exocytosis, but subsequent failure (Fig. 3c). Studying the C_m decline after exocytosis, we observed normal endocytic membrane retrieval (Fig. 3d).

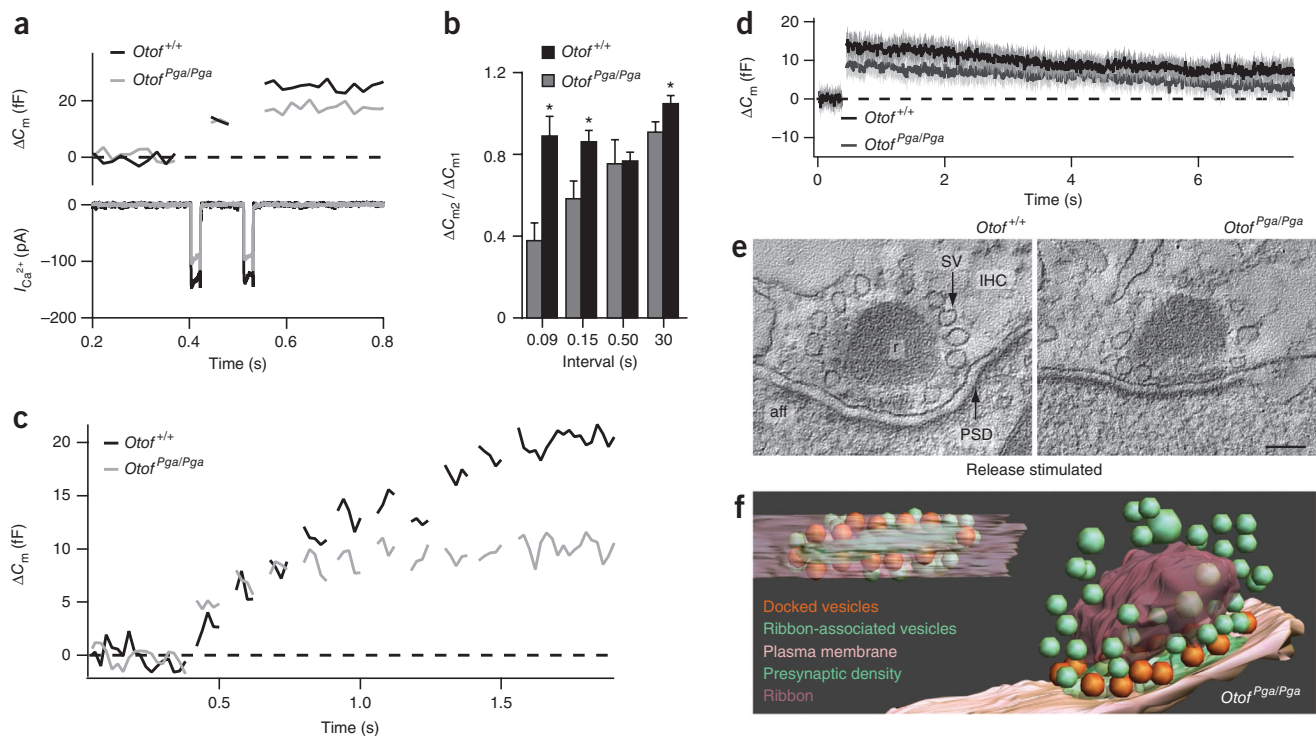


Figure 3 Fatigue of exocytosis, slowed RRP refilling are seen in *Otof^{Pgal/Pgal}* IHCs, but docking and endocytic membrane retrieval are unaltered. (a) Representative low pass-filtered ΔC_m traces (top) and Ca^{2+} currents (bottom) obtained in *Otof^{+/+}* and *Otof^{Pgal/Pgal}* IHCs in response to a pair of 20-ms depolarizations to -14 mV, which were separated by 89 ms. (b) Mean ratios of exocytic ΔC_m (\pm s.e.m.) in response to the second depolarization (ΔC_{m2}) over the first (ΔC_{m1}) as a function of interstimulus interval for *Otof^{+/+}* ($n = 13$) and *Otof^{Pgal/Pgal}* ($n = 15$) IHCs. * $P < 0.05$. (c) Average ΔC_m traces recorded in response to 8-Hz trains of 10-ms depolarizations in *Otof^{+/+}* and *Otof^{Pgal/Pgal}* IHCs. (d) Mean endocytic membrane capacitance changes measured in response to 20-ms depolarization pulses to peak Ca^{2+} current potential at 2 mM $[Ca^{2+}]_e$ in *Otof^{Pgal/Pgal}* ($n = 5$) and in *Otof^{+/+}* IHCs ($n = 12$). In an additional dataset, 11 *Otof^{Pgal/Pgal}* IHCs acquired in 10 mM $[Ca^{2+}]_e$ also showed robust endocytosis (data not shown). (e) Tomogram sections of ribbon synapses in *Otof^{+/+}* (left) and *Otof^{Pgal/Pgal}* (right) IHCs fixed in stimulatory conditions. (f) Three-dimensional model of an *Otof^{Pgal/Pgal}* synapse fixed in stimulatory conditions seen from the synaptic cleft (left) and the side (right). Scale bar represents 100 nm.

Normal synaptic ultrastructure in *Otof^{Pgal/Pgal}* IHCs

To determine whether a docking or a priming defect underlies the impairment of vesicle replenishment at *Otof^{Pgal/Pgal}* IHC synapses, we studied their ultrastructure using electron microscopy. Both electron microscopy of single ultrathin sections (perpendicular to the plasma membrane and the long axis of the ribbon; **Supplementary Fig. 2**) and electron tomography (**Fig. 3e–f** and **Supplementary Movies 1** and **2**) were performed. Organs of Corti were chemically fixed after either prolonged stimulation (40 mM $[K^+]_e$ and 5 mM $[Ca^{2+}]_e$) or inhibition (nominally Ca^{2+} free, 5 mM $[EGTA]_e$ and 5 mM $[K^+]_e$) of exocytosis. We quantified the number of membrane-proximal vesicles (docked, see below) and total ribbon-associated vesicles in electron micrographs of mid-synaptic ultrathin sections of each group (**Supplementary Fig. 2** and **Supplementary Table 3**). We found a significant reduction in the mean number of membrane-proximal vesicles per ribbon synapse section in stimulated synapses of both genotypes (*Otof^{+/+}*, 1.3 ± 0.2 ; *Otof^{Pgal/Pgal}*, 1.5 ± 0.1 ; $n = 27$ and 41 synapses, respectively) when compared with inhibiting conditions (*Otof^{+/+}*, 1.8 ± 0.1 ; *Otof^{Pgal/Pgal}*, 1.9 ± 0.1 ; $n = 36$ and 31 synapses, respectively; $P < 0.05$ for both genotypes). However, we did not detect significant differences in the number of membrane-proximal vesicles between *Otof^{Pgal/Pgal}* and *Otof^{+/+}* IHC synapses in either inhibitory ($P = 0.26$) or stimulatory ($P = 0.26$) conditions (**Supplementary Fig. 2** and **Supplementary Table 3**).

We used high-resolution electron tomography (**Fig. 3e,f**) to measure the distance of membrane-proximal synaptic vesicles (**Fig. 3f**)

from the plasma membrane under both conditions. The average membrane-membrane distance was approximately 6 nm regardless of condition or genotype (**Supplementary Table 3**), which is compatible with the notions that the membrane-proximal vesicles were physically docked and that vesicle docking is intact at *Otof^{Pgal/Pgal}* IHC synapses even during continuous strong stimulation. Although we cannot completely rule out a trafficking/docking phenotype that may have been masked by strong stimulation compensating for the otoferlin defect, we prefer the interpretation that impaired priming underlies the defective vesicle replenishment.

Reduced rates and maintained size variability of EPSCs

The stark contrast between the absence of auditory neuron population responses *in vivo* (**Fig. 1**) and normal RRP exocytosis after sufficient resting reported by C_m measurements *in vitro* in *Otof^{Pgal/Pgal}* mice led us to test postsynaptic function. We made patch-clamp recordings from postsynaptic boutons of SGNs in mice with different *Otof* genotypes at postnatal day 8–10 (**Fig. 4**). These measurements revealed the occurrence of excitatory postsynaptic currents (EPSCs) of variable size and shape in *Otof^{Pgal/Pgal}* mice, although at lower rates when compared with *Otof^{+/+}* mice (**Fig. 4a,b**). We pooled the data from recordings in 5.8 and 40 mM $[K^+]_e$, as previous work^{8,32,33} has shown that the mean EPSC amplitude is stimulus independent in rat SGNs. As in immature rat SGNs, we found a substantial fraction of multiphasic EPSCs in mice of both genotypes (10% of 644 EPSCs in *Otof^{+/+}* and 16% of 279 EPSCs in *Otof^{Pgal/Pgal}*). Monophasic EPSCs of *Otof^{Pgal/Pgal}*

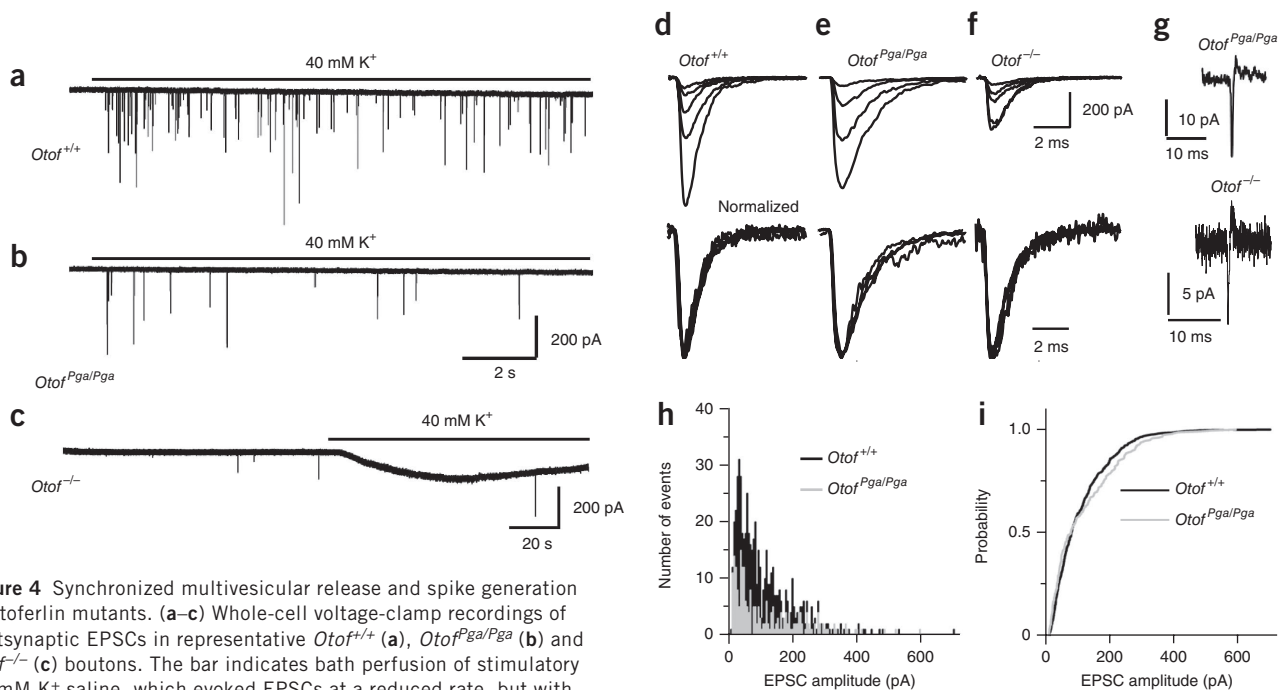


Figure 4 Synchronized multivesicular release and spike generation in otoferlin mutants. (a–c) Whole-cell voltage-clamp recordings of postsynaptic EPSCs in representative *Otof*^{+/+} (a), *Otof*^{Pga/Pga} (b) and *Otof*^{-/-} (c) boutons. The bar indicates bath perfusion of stimulatory 40 mM K⁺ saline, which evoked EPSCs at a reduced rate, but with size variability, in *Otof*^{Pga/Pga} (note the different time scale in c) and *Otof*^{-/-}. (d–f) Enlarged absolute (top) and normalized (bottom) EPSCs: kinetically homogeneous, but variably sized, EPSCs. (g) Action currents recorded from terminals of *Otof*^{Pga/Pga} (top) and *Otof*^{-/-} (bottom) mice. (h) Pooled amplitude distributions for monophasic EPSCs of all *Otof*^{+/+} and *Otof*^{Pga/Pga} boutons ($n = 6$ cells and 577 EPSCs, and $n = 4$ cells and 235 EPSCs, respectively). Bin width in the histogram is 5 pA. (i) There was no significant difference in average EPSC size for the two genotypes in the cumulative amplitude distributions ($P = 0.14$).

mice showed fast rise without obvious steps (Fig. 4d,e). Large EPSCs with kinetics identical to small EPSCs have been proposed to reflect highly synchronized multivesicular release³². The amplitude distribution of monophasic EPSCs was not significantly different in *Otof*^{Pga/Pga} SGNs as compared to controls (Kolmogorov-Smirnov test, $P = 0.14$; Fig. 4h,i). Moreover, we detected action potential generation by recording action currents in the loose-patch configuration (Fig. 4g). Together, these results suggest that *Otof*^{Pga/Pga} synapses should be capable of encoding sound into spiking activity in auditory nerve fibers, albeit at lower rates than wild-type synapses.

We recorded from SGNs of *Otof*^{-/-} mice of the same age and observed variably sized EPSCs at a very low rate ($n = 5$ *Otof*^{-/-} SGNs; Fig. 4c), indicating that the observed ΔC_m in *Otof*^{-/-} IHCs (ref. 23 and Fig. 2) did indeed report synaptic transmitter release. We also observed action currents in the loose-patch configuration (Fig. 4g). In conclusion, transmitter release and postsynaptic spike generation in SGNs occur in otoferlin mutants and EPSC variability was also observed in the absence of otoferlin.

Systems consequences of impaired vesicle replenishment

How can the partial defect at the ribbon synapse that we found *in vitro* lead to such severe hearing impairment? We reasoned that spontaneous transmitter release in the absence of sound could steadily deplete the RRP in *Otof*^{Pga/Pga} IHCs as a result of impaired vesicle supply. To test this hypothesis, we performed extracellular recordings with microelectrodes targeted to the cochlear nucleus and the auditory nerve^{34,35}. Sound-driven single-neuron activity was scarce and only found at high stimulus intensities (>100 dB at 10 Hz). Broadband stimulation (white-noise bursts) of sound-responsive neurons in *Otof*^{Pga/Pga} mice revealed very low sound-driven spike rates, lacking the peak at sound onset typically observed in *Otof*^{+/+} auditory nerve fibers and bushy cells (Fig. 5a).

Sound-responsive neurons in *Otof*^{Pga/Pga} mice, unlike in *Otof*^{+/+} mice, could not be further classified into auditory nerve fibers and cochlear nucleus neurons on the basis of their response properties³⁴. Thus, we used data from putative auditory nerve fibers and bushy cells from *Otof*^{+/+} mice as controls.

Lowering stimulus rates (<10 Hz) gradually improved sound onset responses (Fig. 5b and Supplementary Fig. 3) and thresholds (Supplementary Fig. 3) in *Otof*^{Pga/Pga} neurons. We favor the interpretation that, at lower stimulus rates, vesicle supply can also build up a standing RRP at *Otof*^{Pga/Pga} IHC synapses. In addition, there was a notable depression in the number of spikes occurring during the first trials of stimulation, especially at high stimulus rates, in *Otof*^{Pga/Pga} neurons (Fig. 5c), whereas such an adaptation was only seen at 10 Hz in *Otof*^{+/+} neurons. Moreover, even at a rate of 1 Hz, 12% of the stimulus presentations failed to evoke spikes in *Otof*^{Pga/Pga} neurons, whereas *Otof*^{+/+} neurons always responded. Finally, *Otof*^{Pga/Pga} neurons had strongly increased latencies and jitter of the first spike for all interstimulus intervals (Fig. 5d). In summary, spiking at sound onset occurred with low reliability and high temporal jitter in *Otof*^{Pga/Pga} neurons, and probably did not allow summation into a sizable auditory population response³⁶, thereby explaining the absence of auditory evoked potentials (Fig. 1), even for increased interstimulus intervals (up to 4 s, data not shown). The distribution of spontaneous spike rates in *Otof*^{Pga/Pga} neurons (mean rate, 4.7 ± 1.0 Hz) differed from that in *Otof*^{+/+} auditory nerve fibers and cochlear nucleus units (23.9 ± 2.7 Hz) in that all units had spontaneous rates below 30 Hz (Supplementary Fig. 3). Irrespective of whether sound-responsive neurons in *Otof*^{Pga/Pga} mice represent auditory nerve fibers or principal neurons of the cochlear nucleus, these *in vivo* data support the hypothesis that auditory fatigue is the result of defective vesicle replenishment at the IHC synapses in *Otof*^{Pga/Pga} mice.

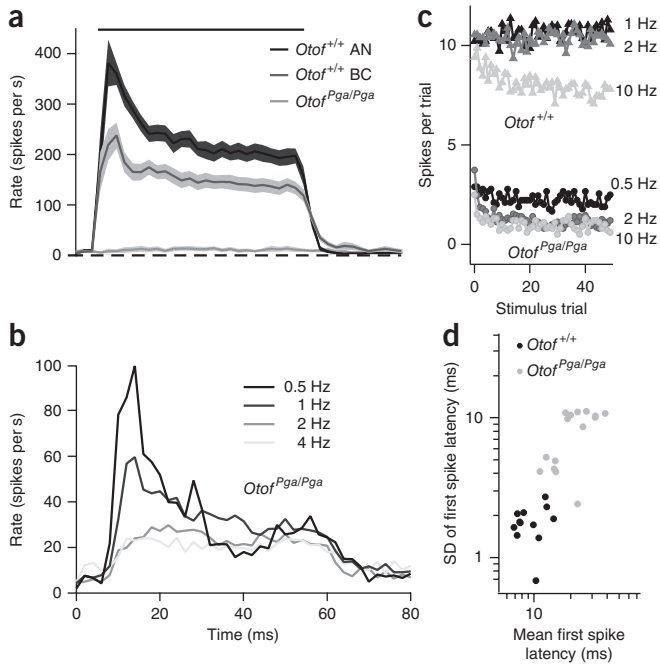


Figure 5 Reduced and fatiguing sound encoding in *Otof^{Pga/Pga}* mice. (a) Mean poststimulus time histograms (\pm s.e.m.) of auditory nerve fibers (AN, $n = 15$, primary-like discharge pattern, depth $>1,000$ μm from the surface of the cochlear nucleus) and bushy cells (BC, $n = 34$, primary-like type response with a depth of $<1,000$ μm or primary-like response with notch discharge pattern) obtained from responses to 10-Hz tone bursts at a characteristic frequency 30 dB above threshold in *Otof^{+/+}* mice and sound-responsive neurons recorded from the region of the cochlear nucleus in *Otof^{Pga/Pga}* mice ($n = 10$, 10-Hz noise bursts at 120–140 dB SPL). (b) Poststimulus time histograms of *Otof^{Pga/Pga}* units stimulated at different rates (0.5–4 Hz, $n = 8$ –13). (c) The number of sound-evoked spikes during the first 50 trials of stimulation in *Otof^{Pga/Pga}* ($n = 15$) and *Otof^{+/+}* ($n = 15$) units. (d) Mean and s.d. of first spike latency in *Otof^{Pga/Pga}* ($n = 14$) and *Otof^{+/+}* ($n = 12$) units.

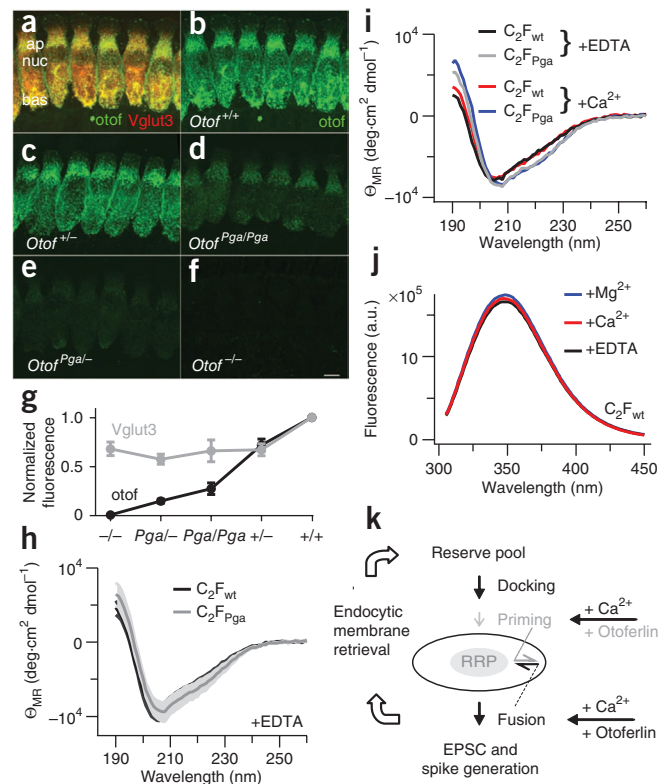
Reduced otoferlin protein levels in *Otof^{Pga/Pga}* IHCs

We next addressed potential molecular mechanisms by which the *pachanga* mutation could affect the function of otoferlin in vesicle priming. We first examined the expression of *Otof* mRNA and protein. *Otof* mRNA levels were not significantly altered in *Otof^{Pga/Pga}* mice, as assessed by real-time PCR (1.6 ± 0.2 -fold of *Otof^{+/+}*, $n = 4$, $P = 0.11$). Localization and protein levels of otoferlin were studied by semi-quantitative optical microscopy of immunolabeled IHCs. We found overlapping distributions of Vglut3 (glutamate transporter of IHC synaptic vesicles^{37–39}) and otoferlin immunofluorescence throughout the cytosol and along the plasma membrane in both *Otof^{+/+}* and *Otof^{Pga/Pga}* IHCs. The latter, however, showed much weaker otoferlin immunofluorescence (Fig. 6). We quantified otoferlin protein levels using antibodies to N- and C-terminal epitopes; binding of either of the antibodies was unlikely to be affected by the point mutation in the C₂F domain. In basolateral and apical IHC compartments, otoferlin protein levels were highest in *Otof^{+/+}*

mice, followed by *Otof^{+/-}*, *Otof^{Pga/Pga}* and then *Otof^{Pga/-}* mice (Fig. 6b–e,g). *Otof^{-/-}* mice (Fig. 6f,g) served as negative controls. Vglut3 immunofluorescence was decreased by approximately 30% in all mutant phenotypes, indicating that the reduction in otoferlin immunofluorescence may be partially attributable to a reduction in synaptic vesicle number in these IHCs (Fig. 6g). Nonetheless, the reduced relative fluorescence (otoferlin/Vglut3) indicates that synaptic vesicles in *Otof^{Pga/-}* and *Otof^{Pga/Pga}* IHCs contain fewer copies of otoferlin. In addition, otoferlin immunofluorescence in *Otof^{Pga/Pga}* IHCs was reduced more strongly at the plasma membrane than in the cytoplasm (Supplementary Fig. 4).

We then examined the effect of the *pachanga* point mutation on the secondary structure of the otoferlin C₂F domain by circular dichroism spectroscopy. We observed slight changes in the circular dichroism spectrum, suggesting that there are minor structural differences between the wild-type and the mutated C₂F domains (Fig. 6h). Adding Ca²⁺ to the protein solution had no effect on the circular dichroism spectra of wild-type and mutated C₂F domains (Fig. 6i) or on tryptophane autofluorescence of the wild-type C₂F

Figure 6 The *pachanga* mutation causes a reduction in otoferlin protein levels and a change in secondary structure. (a–f) Projected confocal sections of apical cochlear turns of different genotypes following immunolabeling for otoferlin (N terminal, green) and Vglut3 (shown only in a, red) processed under identical conditions. ap, apical; bas, basolateral; nuc, nucleus. Scale bar represents 5 μm . (g) Fluorescence intensity averaged over an apical and a basal cytosolic region in either channel for the different genotypes. (h,i) Circular dichroism spectroscopy of purified wild-type and *pachanga* C₂F domains, averaged traces (\pm s.e.m.) in the presence of EDTA (h) and sample traces in the presence of EDTA or Ca²⁺ (i). (j) Tryptophane autofluorescence of purified wild-type C₂F domain, single traces in the presence of EDTA, Ca²⁺ and Mg²⁺. (k) Proposed functions of otoferlin in hair cell exocytosis. We propose that there is a defect in priming in *Otof^{Pga/Pga}* mice, but docking, stabilization of a normal RRP (under release-inhibiting conditions), Ca²⁺-triggered fusion, EPSC and spike generation, and endocytic membrane retrieval seem to function normally in *Otof^{Pga/Pga}* IHCs. If, however, consumption as a result of spontaneous and evoked release is as high as *in vivo*, a standing RRP cannot be maintained in *Otof^{Pga/Pga}* IHCs (gray ellipse versus black ellipse). Previous work²³ and these results suggest that otoferlin and Ca²⁺ act on both vesicle priming and fusion.



domain (Fig. 6j), indicating a lack of Ca^{2+} binding. Moreover, we did not observe Ca^{2+} -dependent phospholipid binding (Supplementary Fig. 4) for either the wild-type or the mutated C_2F domain. We concluded that lower protein levels of otoferlin, potentially together with minor structural changes and impairment of protein-protein interactions, but not alteration of Ca^{2+} or phospholipid binding, contribute to the auditory phenotype of *Otof^{Pga/Pga}* mice. Potential mechanisms for the lower otoferlin protein levels in *Otof^{Pga/Pga}* IHC include a higher incidence of misfolding during protein synthesis, leading to direct degradation, and decreased protein stability, resulting in faster degradation.

DISCUSSION

The IHC ribbon synapse outperforms other synapses with respect to synaptic vesicle replenishment capacity. We characterized, to the best of our knowledge, the first known mutation that selectively affects this process in IHCs and identified otoferlin as a component of the underlying molecular machinery. The mutation impairs vesicle replenishment most likely by reducing otoferlin protein levels and potentially by interfering with protein-protein interactions. Our analysis of *Otof^{Pga/Pga}* IHC synapses indicates that compromised vesicle replenishment leads to auditory fatigue and profound hearing impairment, as a sufficiently large standing RRP cannot be maintained during synaptic activity *in vivo*.

We took advantage of the maintenance of Ca^{2+} influx-triggered fusion of readily releasable vesicles in the *Otof^{Pga/Pga}* mutant²⁶. Our results provide evidence for an additional function of otoferlin in vesicle priming (Fig. 6k) and argue against potential defects in vesicle trafficking and docking, synaptic Ca^{2+} signaling, fusion and transmitter release, and endocytic membrane retrieval in *Otof^{Pga/Pga}* IHCs. Currently we cannot exclude an impairment of active zone clearance after synaptic fusion⁴⁰, as that would be functionally indistinguishable. It is possible, although less likely, that the reduced sustained exocytosis and smaller fast flash response result from a major contribution of a slowly releasable pool of vesicles (docked at greater distance to Ca^{2+} channels⁴¹ or using a different Ca^{2+} sensor⁴²) to sustained exocytosis and from selectively impaired exocytosis of those slowly releasable vesicles in *Otof^{Pga/Pga}* IHCs.

On the basis of our *in vitro* recordings, we conclude that a normal standing RRP can be established in *Otof^{Pga/Pga}* IHCs as long as enough time is provided for vesicle replenishment. Most likely, a normal number of 'slots' (close to Ca^{2+} channels^{27,43}) are available for releasable vesicles, which provide an intact Ca^{2+} influx-exocytosis coupling, as indicated by normal RRP release kinetics. We favor the hypothesis that, *in vivo*, ongoing exocytosis in the absence of sound stimulation leads to steady vesicle consumption and thus a smaller standing RRP in *Otof^{Pga/Pga}* IHCs. This reduced RRP and the slower speed of vesicle supply probably limit the rates of transmitter release and subsequent neuronal spiking on sound stimulation.

In addition to accelerating vesicle replenishment, otoferlin has been implicated in Ca^{2+} -triggered fusion²³. Does otoferlin then assume multiple functions in IHC exocytosis? In the absence of otoferlin, a stronger impairment in vesicle replenishment than that observed in *Otof^{Pga/Pga}* IHCs could arise. However, the complete lack of fast exocytosis even after long periods of rest and the partially preserved slow exocytosis in *Otof^{-/-}* IHCs cannot simply be explained this way and instead indicates an additional requirement for otoferlin in fusion²³ (Fig. 6k). Although the perturbation of vesicle replenishment and fusion causes a complete loss of fast exocytosis in *Otof^{-/-}* IHCs, the functionality of the *pachanga* mutant protein and the number of protein copies present on synaptic vesicles apparently suffice to

support fast fusion in *Otof^{Pga/Pga}* IHCs, but fail to maintain efficient vesicle replenishment. Regarding this dual-function hypothesis for otoferlin, it is noteworthy that a function upstream of fusion was recently also reported for synaptotagmin 1 (ref. 44).

Otoferlin, which seems to be absent from other synapses such as retinal ribbon synapses³⁵, is an attractive candidate for conferring the fast vesicle replenishment capacity to IHCs. During strong *in vitro* stimulation, IHCs sustain a near constant exocytosis rate of hundreds (700 in this study) of vesicles per s per active zone or tens of vesicles per s per 'RRP slot' for at least 1 s during ongoing stimulation. The vesicle supply rates of wild-type IHCs exceed those of rat retinal bipolar cells by almost an order of magnitude (70 vesicles per s per active zone), despite comparable synaptic ultrastructure and RRP size of bipolar cell active zones¹⁴. Estimates of maximal vesicle supply in retinal photoreceptors of the salamander, which have larger active zones than IHCs and bipolar cells⁴⁵, amount to approximately 200 vesicles per s per active zone^{13,15}. Notably, sustained exocytosis of mouse vestibular hair cells operates at lower rates than in cochlear IHCs and is reduced on deletion of otoferlin⁴⁶. Different rates of vesicle supply and different effects of otoferlin deletion in auditory and vestibular hair cells might reflect the involvement of distinct proteins that co-determine the replenishment rate. Unlike retinal and vestibular junctions, each postsynaptic auditory neuron is driven by a single IHC active zone and fires up to hundreds of hertz during ongoing acoustic stimulation (for review, see ref. 2), requiring similar or higher rates of release.

How can one reconcile the substantial sustained exocytosis (200 vesicles per s per active zone) observed in IHCs of *Otof^{Pga/Pga}* mice *in vitro* with the severe impairment of sound encoding *in vivo*? If other aspects of cochlear function apart from vesicle replenishment are intact, as indicated by normal otoacoustic emissions, cochlear microphonics and summing potentials, then why were high sound pressure levels required to elicit neuronal responses? Although alternative interpretations cannot be ruled out at present, we favor the hypothesis that the requirement for otoferlin may be most critical for maintaining a standing RRP during weak stimulation. The Ca^{2+} signal elicited by strong stimulation, saturating depolarizations and elevated $[\text{Ca}^{2+}]_e$ (Fig. 2), high $[\text{K}^+]_e$ (Figs. 3 and 4), and high sound intensities (Fig. 5), might have been high enough to enhance vesicle supply and support substantial transmission even in *Otof^{Pga/Pga}* mice. It is tempting to speculate that the multi- C_2 domain protein otoferlin endows vesicle supply at the IHC synapse with high Ca^{2+} sensitivity to enable sufficient vesicle replenishment during weak stimulation. Future studies are required to further characterize the Ca^{2+} dependence of vesicle supply in IHCs.

METHODS

Methods and any associated references are available in the online version of the paper at <http://www.nature.com/natureneuroscience/>.

Note: Supplementary information is available on the Nature Neuroscience website.

ACKNOWLEDGMENTS

We would like to thank E. Glowatzki and D. Khimich for teaching us the postsynaptic patch clamp, K. Tittman, D. Fasshauer and R. Jahn for advice and support for protein biochemistry, C.P. Richter and M.A. Cheatham for advice on the electrocochleography, A. Leonov and C. Griesinger for the DM-nitrophen, P. Jonas for the parvalbumin taqman probe, members of the InnerEarLab for discussion, M. Rutherford, J. Singer, E. Neher, J. Siegel, P. Heil, T. Sakaba, R. Nouvian, A. Lysakowski and A. Lee for comments on the manuscript and C. Rüdiger, S. Blume, N. Dankenbrink-Werder and M. Köppler for expert technical assistance. This work was supported by a fellowship of the Alexander von Humboldt Foundation to T.P., a fellowship of the Boehringer Ingelheim Fonds to K.R., a fellowship of MED-EL company to H.T., grants from the German Research

Foundation (Center for Molecular Physiology of the Brain, T.M. and N.B.; Fellowship to N.S.), the European Commission (Eurohear, T.M.), the Max-Planck-Society (Tandemproject, T.M. and N.B.), the German Ministry for Education and Science via the Bernstein Focus Neurotechnology Goettingen (grant no. 01GQ0810 to T.M.), the State of Lower Saxony ('VW-Vorab' to T.M. and Christoph Matthias), and the US National Institutes of Health (DC007704, U.M.).

AUTHOR CONTRIBUTIONS

The study was designed by T.M., T.P., U.M., N.S., E.R. and N.B. T.P. carried out the IHC patch clamp and flash photolysis, extracellular postsynaptic recordings and immunohistochemistry and contributed to the electron microscopy. L.L. performed *in vivo* single-unit recordings, electrocochleography and auditory brainstem responses. K.R. carried out real-time PCR, protein purification, circular dichroism spectroscopy, fluorimetry and the floatation assay. H.T. performed postsynaptic recordings. M.S. carried out the ENU screen and initial auditory testing. D.R. performed electron microscopy. T.F. carried out Ca²⁺ imaging. N.S. performed *in vivo* physiology. E.R. generated the knockout mice. J.S.B. and L.M.T. started the ENU screen. T.M. and T.P. prepared the manuscript.

COMPETING FINANCIAL INTERESTS

The authors declare no competing financial interests.

Published online at <http://www.nature.com/natureneuroscience/>.

Reprints and permissions information is available online at <http://www.nature.com/reprintsandpermissions/>.

- Kiang, N.Y.-S., Watanabe, T., Thomas, E.C. & Clark, L.F. *Discharge Pattern of Single Fibers in the Cat's Auditory Nerve* (MIT Press, Cambridge, Massachusetts, 1965).
- Geisler, C.D. *From Sound to Synapse* (Oxford University Press, New York, 1998).
- Parsons, T.D., Lenzi, D., Almers, W. & Roberts, W.M. Calcium-triggered exocytosis and endocytosis in an isolated presynaptic cell: capacitance measurements in saccular hair cells. *Neuron* **13**, 875–883 (1994).
- Moser, T. & Beutner, D. Kinetics of exocytosis and endocytosis at the cochlear inner hair cell afferent synapse of the mouse. *Proc. Natl. Acad. Sci. USA* **97**, 883–888 (2000).
- Schnee, M.E., Lawton, D.M., Furness, D.N., Benke, T.A. & Ricci, A.J. Auditory hair cell-afferent fiber synapses are specialized to operate at their best frequencies. *Neuron* **47**, 243–254 (2005).
- Griesinger, C.B., Richards, C.D. & Ashmore, J.F. Fast vesicle replenishment allows indefatigable signaling at the first auditory synapse. *Nature* **435**, 212–215 (2005).
- Keen, E.C. & Hudspeth, A.J. Transfer characteristics of the hair cell's afferent synapse. *Proc. Natl. Acad. Sci. USA* **103**, 5537–5542 (2006).
- Goutman, J.D. & Glowatzki, E. Time course and calcium dependence of transmitter release at a single ribbon synapse. *Proc. Natl. Acad. Sci. USA* **104**, 16341–16346 (2007).
- von Gersdorff, H. & Matthews, G. Depletion and replenishment of vesicle pools at a ribbon-type synaptic terminal. *J. Neurosci.* **17**, 1919–1927 (1997).
- Gomis, A., Burrone, J. & Lagnado, L. Two actions of calcium regulate the supply of releasable vesicles at the ribbon synapse of retinal bipolar cells. *J. Neurosci.* **19**, 6309–6317 (1999).
- Zenisek, D., Steyer, J.A. & Almers, W. Transport, capture and exocytosis of single synaptic vesicles at active zones. *Nature* **406**, 849–854 (2000).
- Thoreson, W.B., Rabl, K., Townes-Anderson, E. & Heidelberger, R. A highly Ca²⁺-sensitive pool of vesicles contributes to linearity at the rod photoreceptor ribbon synapse. *Neuron* **42**, 595–605 (2004).
- Rabl, K., Cadetti, L. & Thoreson, W.B. Kinetics of exocytosis is faster in cones than in rods. *J. Neurosci.* **25**, 4633–4640 (2005).
- Singer, J.H. & Diamond, J.S. Vesicle depletion and synaptic depression at a mammalian ribbon synapse. *J. Neurophysiol.* **95**, 3191–3198 (2006).
- Jackman, S.L. *et al.* Role of the synaptic ribbon in transmitting the cone light response. *Nat. Neurosci.* **12**, 303–310 (2009).
- Hosoi, N., Sakaba, T. & Neher, E. Quantitative analysis of calcium-dependent vesicle recruitment and its functional role at the calyx of Held synapse. *J. Neurosci.* **27**, 14286–14298 (2007).
- Saviane, C. & Silver, R.A. Fast vesicle reloading and a large pool sustain high bandwidth transmission at a central synapse. *Nature* **439**, 983–987 (2006).
- Khimich, D. *et al.* Hair cell synaptic ribbons are essential for synchronous auditory signaling. *Nature* **434**, 889–894 (2005).
- Moser, T., Neef, A. & Khimich, D. Mechanisms underlying the temporal precision of sound coding at the inner hair cell ribbon synapse. *J. Physiol. (Lond.)* **576**, 55–62 (2006).
- Wittig, J.H. Jr. & Parsons, T.D. Synaptic ribbon enables temporal precision of hair cell afferent synapse by increasing the number of readily releasable vesicles: a modeling study. *J. Neurophysiol.* **100**, 1724–1739 (2008).
- Eisen, M.D., Spassova, M. & Parsons, T.D. Large releasable pool of synaptic vesicles in chick cochlear hair cells. *J. Neurophysiol.* **91**, 2422–2428 (2004).
- Johnson, S.L., Marcotti, W. & Kros, C.J. Increase in efficiency and reduction in Ca²⁺ dependence of exocytosis during development of mouse inner hair cells. *J. Physiol. (Lond.)* **563**, 177–191 (2005).
- Roux, I. *et al.* Otoferlin, defective in a human deafness form, is essential for exocytosis at the auditory ribbon synapse. *Cell* **127**, 277–289 (2006).
- Roux, I. *et al.* Myosin VI is required for the proper maturation and function of inner hair cell ribbon synapses. *Hum. Mol. Genet.* **18**, 4615–4628 (2009).
- Heidrych, P. *et al.* Otoferlin interacts with myosin VI: implications for maintenance of the basolateral synaptic structure of the inner hair cell. *Hum. Mol. Genet.* **18**, 2779–2790 (2009).
- Schwander, M. *et al.* A forward genetics screen in mice identifies recessive deafness traits and reveals that pejvakin is essential for outer hair cell function. *J. Neurosci.* **27**, 2163–2175 (2007).
- Brandt, A., Khimich, D. & Moser, T. Few CaV1.3 channels regulate the exocytosis of a synaptic vesicle at the hair cell ribbon synapse. *J. Neurosci.* **25**, 11577–11585 (2005).
- Frank, T., Khimich, D., Neef, A. & Moser, T. Mechanisms contributing to synaptic Ca²⁺ signals and their heterogeneity in hair cells. *Proc. Natl. Acad. Sci. USA* **106**, 4483–4488 (2009).
- Spassova, M.A. *et al.* Evidence that rapid vesicle replenishment of the synaptic ribbon mediates recovery from short-term adaptation at the hair cell afferent synapse. *J. Assoc. Res. Otolaryngol.* **5**, 376–390 (2004).
- Meyer, A.C. *et al.* Tuning of synapse number, structure and function in the cochlea. *Nat. Neurosci.* **12**, 444–453 (2009).
- Li, G.L., Keen, E., Andor-Ardo, D., Hudspeth, A.J. & von Gersdorff, H. The unitary event underlying multiquantal EPSCs at a hair cell's ribbon synapse. *J. Neurosci.* **29**, 7558–7568 (2009).
- Glowatzki, E. & Fuchs, P.A. Transmitter release at the hair cell ribbon synapse. *Nat. Neurosci.* **5**, 147–154 (2002).
- Grant, L., Yi, E. & Glowatzki, E. Two modes of release shape the postsynaptic response at the inner hair cell ribbon synapse. *J. Neurosci.* **30**, 4210–4220 (2010).
- Taberner, A.M. & Liberman, M.C. Response properties of single auditory nerve fibers in the mouse. *J. Neurophysiol.* **93**, 557–569 (2005).
- Strenzke, N. *et al.* Complexin-I is required for high-fidelity transmission at the endbulb of held auditory synapse. *J. Neurosci.* **29**, 7991–8004 (2009).
- Starr, A., Michalewski, H.J., Feng, G. & Moser, T. Perspectives on auditory neuropathy: disorders of inner hair cell, auditory nerve and their synapse. in *The Senses: a Comprehensive Reference* (eds Dallos, P. & Oertel, D.) 397–412 (Elsevier, Amsterdam, 2008).
- Obholzer, N. *et al.* Vesicular glutamate transporter 3 is required for synaptic transmission in zebrafish hair cells. *J. Neurosci.* **28**, 2110–2118 (2008).
- Seal, R.P. *et al.* Sensorineural deafness and seizures in mice lacking vesicular glutamate transporter 3. *Neuron* **57**, 263–275 (2008).
- Ruel, J. *et al.* Impairment of SLC17A8 encoding vesicular glutamate transporter-3, VGLUT3, underlies nonsyndromic deafness DFNA25 and inner hair cell dysfunction in null mice. *Am. J. Hum. Genet.* **83**, 278–292 (2008).
- Hosoi, N., Holt, M. & Sakaba, T. Calcium dependence of exo- and endocytotic coupling at a glutamatergic synapse. *Neuron* **63**, 216–229 (2009).
- Wadel, K., Neher, E. & Sakaba, T. The coupling between synaptic vesicles and Ca²⁺ channels determines fast neurotransmitter release. *Neuron* **53**, 563–575 (2007).
- Wölfel, M., Lou, X. & Schneggenburger, R. A mechanism intrinsic to the vesicle fusion machinery determines fast and slow transmitter release at a large CNS synapse. *J. Neurosci.* **27**, 3198–3210 (2007).
- Neef, J. *et al.* The Ca²⁺ channel subunit beta2 regulates Ca²⁺ channel abundance and function in inner hair cells and is required for hearing. *J. Neurosci.* **29**, 10730–10740 (2009).
- de Wit, H. *et al.* Synaptotagmin-1 docks secretory vesicles to syntaxin-1/SNAP-25 exocytotic complexes. *Cell* **138**, 935–946 (2009).
- Sterling, P. & Matthews, G. Structure and function of ribbon synapses. *Trends Neurosci.* **28**, 20–29 (2005).
- Dulon, D., Safieddine, S., Jones, S.M. & Petit, C. Otoferlin is critical for a highly sensitive and linear calcium-dependent exocytosis at vestibular hair cell ribbon synapses. *J. Neurosci.* **29**, 10474–10487 (2009).
- Neef, A. *et al.* Probing the mechanism of exocytosis at the hair cell ribbon synapse. *J. Neurosci.* **27**, 12933–12944 (2007).
- Beutner, D., Voets, T., Neher, E. & Moser, T. Calcium dependence of exocytosis and endocytosis at the cochlear inner hair cell afferent synapse. *Neuron* **29**, 681–690 (2001).



ONLINE METHODS

Animals. Mice aged 1 (postsynaptic patch clamp), 2–3 (presynaptic patch clamp and immunohistochemistry, auditory brainstem responses) and 3–5 weeks (*in vivo* auditory physiology) were used. The generation of *Otof*^{-/-} mice will be described elsewhere (E.R., Bresee, C., Neef, J., Nair, R., Bulankina, A., K.R., Koch, M., N.B., Rhee, J.S., Kügler, S., Brigande, J. and T.M., unpublished observations). Generation of *Otof*^{Pga/Pga} mice was described previously²⁶. C57BL/6 mice were used as control animals. Animal handling and experiments complied with national animal care guidelines and were approved by the University of Goettingen Board for Animal Welfare and the Animal Welfare Office of the state of Lower Saxony.

Patch-clamp recordings. IHCs from the apical coils of freshly dissected organs of Corti were patch clamped in the perforated-patch (depolarizations) or whole-cell (flash photolysis, Ca²⁺ imaging) configuration as described previously^{4,48}. The pipette solutions for perforated-patch experiments contained 130 mM cesium gluconate, 10 mM tetraethylammonium-chloride (TEA-Cl), 10 mM 4-aminopyridine (Merck), 1 mM MgCl₂, 10 mM cesium HEPES (pH 7.17) and 300 μg ml⁻¹ amphotericin B (Calbiochem). The pipette solution for flash photolysis contained 120 mM cesium gluconate, 20 mM TEA-Cl, 20 mM cesium HEPES (pH 7.2), 0.3 mM mag-fura-2 (Invitrogen), 10 mM DM-nitrophen (gift of A. Leonov and C. Griesinger, Göttingen), 5 mM 1,3-diaminopropan-2-ol-tetraacetic acid and 10 mM CaCl₂. The pipette solution for Ca²⁺ imaging contained 126 mM cesium glutamate, 13 mM TEA-Cl, 20 mM cesium HEPES, 1 mM MgCl₂, 0.1 mM CaCl₂, 2 mM MgATP, 0.3 mM NaGTP, 2 mM EGTA and 0.4 mM Fluo-5N (Penta-K⁺ salt, Invitrogen), pH 7.0. The extracellular solutions contained 113 mM NaCl (102 mM for Ca²⁺ imaging), 35 mM TEA-Cl, 2.8 mM KCl, 2 mM CaCl₂ (10 mM for flash-photolysis and some perforated-patch experiments, 5 mM for Ca²⁺ imaging), 1 mM MgCl₂, 10 mM sodium HEPES, 1 mM CsCl and 11.1 mM D-glucose (pH 7.2).

Loose-patch and whole-cell recordings from postsynaptic boutons were performed as described previously³² using pipettes with small tip-opening (8–15 MΩ following pressure polishing⁴⁹), a pipette solution containing 150 mM KCl, 3.5 mM MgCl₂, 0.1 mM CaCl₂, 5 mM EGTA, 5 mM potassium HEPES and 2.5 mM Na₂ATP (pH 7.2) and an extracellular solution containing 5.8 mM KCl, 155 mM NaCl, 0.9 mM MgCl₂, 1.3 mM CaCl₂, 0.7 mM NaH₂PO₄, 5.6 mM D-glucose, 10 mM sodium HEPES (pH 7.4). In most recordings, tetrodotoxin (1–2 μM) was added to block voltage-gated sodium channels. All chemicals were obtained from Sigma-Aldrich, unless stated otherwise. EPC-9 or EPC-10 amplifiers (HEKA Electronics), controlled by Pulse or Patchmaster software, were used to sample and filter currents at 20 and 5 kHz, respectively. We measured ΔC_m as previously described⁴ using depolarizations of different durations to peak Ca²⁺ current potential at intervals of 30–60 s. ΔC_m was estimated as the difference of the mean C_m after depolarization and the mean pre-pulse C_m (the initial 40 ms after the depolarization were skipped). Mean ΔC_m and Ca²⁺ current estimates present grand averages calculated from the mean estimates of individual IHCs. In paired-pulse experiments, we used two 20-ms-long pulses with variable inter-stimulus interval: 89, 154 and 504 ms and 30 s. Currents were leak corrected using a P/10-protocol. Recordings were performed at 21–23 °C. Flash photolysis was performed as described⁴⁸.

Confocal imaging of Ca²⁺ signals at hair cell ribbon synapses. Confocal Ca²⁺ imaging was performed as previously described²⁸. Ca²⁺ microdomains were identified in *xy* scans during 200-ms-long depolarizations and further characterized using spot detection (point scan mode of the confocal scanner). During spot detection measurements, the output of the photomultiplier tube (PMT) signal (500 kHz) was temporally averaged to yield an effective sampling rate of 1.85 kHz. Isochronal spot detection measurements were made at the center of a Ca²⁺ microdomain and at the four directly neighboring pixels on each side of the center along each direction of the *x* and *y* axis (130-nm spacing between the neighboring recording locations and the center), each averaged five times. Only the maximum amplitude response was further analyzed. PMT dark current (measured with shutter closed) was subtracted for all measurements. Igor Pro (Wavemetrics) was used for analysis.

Recordings of cochlear potentials (electrocochleography), auditory brainstem responses and single-unit responses. Auditory brainstem response recordings were performed as described previously⁴³. Clicks are presented in dB peak equivalent, and tone and noise bursts in dB sound pressure level.

For electrocochleography, the mouse head was fixed, the bulla was opened from a retroauricular incision, a silver ball-electrode was placed into the round window niche, and the difference potential to a subdermal needle at the vertex was amplified (50 times, custom-built amplifier) and sampled at a rate of 50 kHz for 20 ms. For analysis of CAP and summing potentials, responses to stimuli of inverting polarity were averaged and low-pass filtered (3 kHz) offline using Matlab (Mathworks) software.

Single auditory neuron responses from the ventral cochlear nucleus and auditory nerve were performed essentially as described previously³⁵. On audio-visual detection of spiking activity, units were further characterized by determining their spontaneous rate and responses to 50-ms noise bursts presented at 0.5, 1, 2, 4 or 10 Hz. Attempts to record tuning curves did not yield consistent results in *Otof*^{Pga/Pga} mice because of low spike rates that depended on interstimulus intervals, high thresholds (usually above 100 dB SPL) and broad frequency tuning. Subsequent offline spike detection using Matlab was based on amplitudes, waveform reproducibility and signal-to-noise ratio.

We assume that we recorded mainly from primary units of the cochlear nucleus because they were localized in the auditory nerve/cochlear nucleus region (many of them were too superficial to be auditory nerve fibers), the signal-to-noise ratio and our ability to achieve long recording durations were relatively good, better than in typical auditory nerve recordings, the responses to low-frequency sounds (0.1–2 kHz) were not better than those to higher-frequency sounds, arguing against a vestibular origin, and the responses of individual units did not change after removal of whiskers, arguing against a trigeminal origin.

Spontaneous or sound-evoked responses also differed from wild-type olivocochlear efferents or vestibular neurons⁵⁰. If we indeed recorded from such units, their responses must also have been affected by the mutation.

Immunostaining and confocal microscopy. Immunostaining was performed as previously described¹⁸. For primary antibodies, we used mouse IgG1 antibody to Ctbp2 (BD Biosciences, 1:200), rabbit antibody to GluR2/3 (Chemicon, 1:200), mouse antibody to calbindin (Swant, 1:500), mouse antibody to otoferlin (N terminal, Abcam, 1:500), rabbit antibody to otoferlin (C terminal, Synaptic Systems, 1:500) and rabbit antibody to Vglut3 (Synaptic Systems, 1:500). We used AlexaFluor 488- and AlexaFluor 568-labeled secondary antibodies (Invitrogen, 1:200). For three-dimensional reconstructions of the specimen, *z* axis stacks of two-dimensional images were taken with a step size of 0.5 μm. They are shown in *z* projections, created using ImageJ. Otoferlin and Vglut3 immunofluorescence signals were analyzed in apical and basolateral intracellular regions in maximum projections of confocal IHC sections. They were acquired at identical microscope settings and following parallel immunolabeling with the same procedure used for all genotypes.

Electron microscopy. The organs of Corti (apical cochlear coils) were explanted and exposed to stimulatory or inhibitory conditions for 10–15 min. For stimulation, they were incubated in a depolarizing saline (containing 50 mM KCl, 95 mM NaCl, 1 mM MgCl₂, 5 mM CaCl₂, 10 mM HEPES, 11.1 mM D-glucose, pH 7.2, osmolarity approximately 300 mOsm) at 21–23 °C. For inhibition, the tissue was incubated in a Ca²⁺-free saline (5 mM KCl, 140 mM NaCl, 3 mM MgCl₂, 5 mM EGTA, 10 mM HEPES and 11.1 mM D-glucose, pH 7.2, osmolarity approximately 300 mOsm) on ice. Thereafter, organs of Corti were incubated for 15–20 min in the respective solution supplemented with 4% glutaraldehyde (vol/vol, Electron Microscopy Sciences) at 21–23 °C. Afterwards, they were incubated overnight at 4 °C in 0.1 M cacodylate buffer supplemented with 4% glutaraldehyde. After an additional fixation in 0.1% OsO₄ (vol/vol), the samples were stained with 1% uranyl acetate (vol/vol), and dehydrated in a series of ethanol washes and finally in propylene oxide. They were then embedded in Agar 100 (purchased through Science Services). Thin sections (80 nm) were counterstained with lead citrate and examined using a Philips CM 120 BioTwin transmission electron microscope. Pictures were taken with a TemCam F224A camera (TVIPS) at 20,000-fold magnification.

Quantitative image analysis was performed in iTEM software (Olympus), where we counted ribbon-associated synaptic vesicles (first row of vesicles around the ribbon with less than a vesicle diameter distance from the ribbon surface), membrane-proximal vesicles (synaptic vesicles associated with the active zone within 12 nm of the plasma membrane) and clathrin-coated vesicles.

To compare the number of membrane-proximal vesicles among the genotypes and among stimulatory and inhibitory conditions, we performed permutation tests and Mann-Whitney U tests.

Electron tomography. Sections (200 nm thick) of Agar 100 embedded organs of Corti were decorated with 10 nm colloidal gold particles on both surfaces. Tilt series (unidirectional tilt) were then recorded on a Philips CM120 transmission electron microscope at 27,500 \times magnification using a TVIPS 224A slow-scan CCD camera in unbinned mode. The series were calculated using Etomo and the model was created using Imod program (<http://bio3d.colorado.edu/>). The smallest distance of membrane-proximal vesicles (outer leaflet) to the plasma membrane (inner leaflet) was quantified in the section displaying the closest proximity.

Protein biochemistry. The C₂F domain (amino acids 1,688 to 1,927, NPKD...NEPD) was subcloned as a GST-fusion construct into a pGEX-2T vector. For the *pachanga* variant, the point mutation was introduced by overlap-PCR using the oligonucleotides 5'-GCC AGC AGG AGG GCA AAC AGG ACA CAG AC-3' and 5'-GTC TGT GTC CTG TTT GCC CTC CTG CTG GC-3'. The subcloned C₂F domains were verified by DNA sequencing. Protein expression in BL21-DE3 cells at 16 °C (overnight) and purification of both constructs were performed in parallel. Cells were pelleted at 5,250 g and re-suspended in 20 mM Tris-HCl (pH 7.4), 500 mM NaCl, 2.5 mM reduced glutathione, 5 μ M ATP and 5% ethanol (vol/vol). Then cells were lysed by sonication with a Branson sonifier 250. Cell debris was pelleted at 23,000 g and the protein was purified from the supernatant using glutathione Sepharose 4B. The protein was cleaved from the GST-tag with 10 U ml⁻¹ thrombin overnight, whereas the tag remained bound to the Sepharose beads. The protein solution was dialyzed against 20 mM phosphate buffer pH 7.4 (for EDTA runs in Fig. 6h) or 5 mM Tris-HCl pH 7.4 (for EDTA and Ca²⁺ runs in Fig. 6i–j) at 4 °C, which had been pre-treated with Chelex100 (BioRad). Protein concentration was determined by ultraviolet absorbance at 280 nm.

Circular dichroism spectroscopy was performed on a Chirascan instrument (Applied Photophysics) at 25 °C with a protein concentration of 0.08 mg ml⁻¹

(3 μ M) per run. EDTA or Ca²⁺ was added to a final concentration of 100 μ M, respectively. Ellipticity was measured from 190 nm to 260 nm, controlling for sufficient light transmission by measuring high tension voltage. All spectra were corrected for buffer contributions.

Autofluorescence was measured in a Fluoromax-3 instrument (Jobin Yvon Horiba) with a protein concentration of 2.36 μ M with 295-nm excitation wavelength. Fluorescence emission was recorded from 305 to 450 nm in 1-nm steps with an integration time of 0.2 s, averaging five runs. Ca²⁺ or EDTA was added to a final concentration of 100 μ M.

Real-time PCR. The apical turns of three to four organs of Corti of *Otof^{Pga/Pga}* or *Otof^{+/+}* mice at postnatal day 14 were dissected and mRNA was extracted by Trizol method. This was repeated three more times for each genotype independently. cDNA synthesis was performed using Superscript II reverse transcriptase in supplied buffer with oligo dT and random hexamers as primers. Real-time PCR was conducted in triplicates for each cDNA sample using an Applied Biosystems SDS 7500 thermal cycler and TaqMan Gene Expression Assays for *Otof* (Applied Biosystems, Mm00453306_m1) and for the housekeeping genes *Pvalb* (kindly provided by P. Jonas, Freiburg) and *Tbp* (Mm00446973_m1). To average C_t values from triplicate experiments, we first calculated a linear value from each C_t value ($lin = 2^{-C_t}$). These linear values were averaged and back-transformed into a C_t value ($C_{t, average} = -LN(lin_{average}) / LN2$). Data were analyzed by the $\Delta\Delta C_t$ method.

Data analysis. Data analysis was performed using Matlab, Igor Pro and ImageJ software. Figures were assembled for display using Adobe Photoshop and Illustrator software. Unless otherwise noted, data are expressed as mean \pm s.e.m. Student's unpaired, two-tailed *t* test was used to compare two samples unless stated otherwise.

49. Goodman, M.B. & Lockery, S.R. Pressure polishing: a method for re-shaping patch pipettes during fire polishing. *J. Neurosci. Methods* **100**, 13–15 (2000).
50. McCue, M.P. & Guinan, J. Jr. Acoustically responsive fibers in the vestibular nerve of the cat. *J. Neurosci.* **14**, 6058–6070 (1994).